THE JOURNAL OF PHYSICAL CHEMISTRY LETTERS
A JOURNAL OF THE AMERICAN CHEMICAL SOCIETY

pubs.acs.org/JPCL

Letter

Structurally Resolved Water-Soluble Copper Nanoclusters with NIR TADF Exhibiting Multifunctional Catalytic Activity

Sameeksha Agrawal, Thrisha Swaminathan, Sanyam, Koushik Mandal, Deepak Chopra,* Anirban Mondal,* and Saptarshi Mukherjee*

Cite This: https://doi.org/10.1021/acs.jpclett.6c01437

Read Online

ACCESS | Metrics & More | Article Recommendations | Supporting Information

ABSTRACT: Thermally activated delayed fluorescence (TADF) in metal nanoclusters (MNCs) is an effective strategy to harvest the emission from the excited-triplet states. However, the applications of these TADF-active MNCs are limited by the use of hydrophobic ligands, which generally make these MNCs insoluble. Herein, we report the NIR-TADF emitting CuNCs that are highly water-soluble and display intense-red emission in the solid state. The atomic connectivity of the CuNCs was determined by SC-XRD technique. The delayed fluorescence phenomenon is validated by temperature-dependent photoluminescence studies, and the excited singlet−triplet energy gap (ΔE_{ST}) was experimentally estimated to be ∼98 meV, thereby substantiating the TADF mechanism. DFT calculations performed on the crystal geometry of the CuNCs further attested to the TADF mechanism along with the associated charge-transfer dynamics. Additionally, the CuNCs demonstrate excellent catalytic activity involving the reduction of ferricyanide and Methylene Blue, highlighting their multifunctional applications in the aqueous phase.

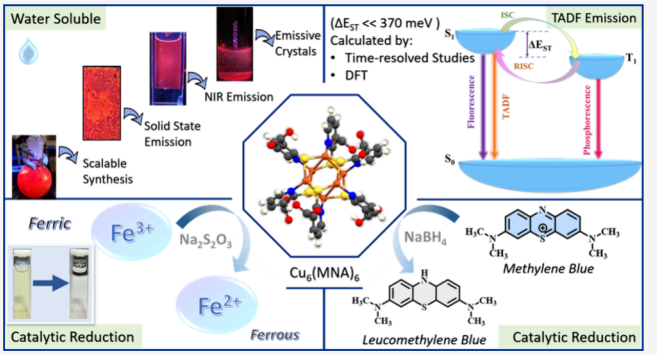

Atomically precise metal nanoclusters (MNCs) have gained significant interest due to their exceptional photophysics and multifaceted applications.[1−9] However, their applications are limited by relatively low photoluminescence quantum yields (PLQYs), driving efforts to understand the emission mechanism in MNCs.[10−12] Initially, this was linked to the semiconductor quantum dots, as both exhibit a similar quantum confinement effect. However, recent studies support their molecule-like nature, specifically because of the involvement of triplet states in many MNCs.[13] Harvesting triplet state emission in MNCs is key to enhancing the PLQYs, as most of the triplet-state population undergoes nonradiative decay because of the spin-forbidden transitions.[14,15] Thermally activated delayed fluorescence (TADF)-based materials have garnered significant attention because of the greater thermal emission stability, photoluminescence tuning, and enhanced emission efficiency.[16,17] Although TADF processes are common for organic emitters, this phenomenon is still rare for MNCs.[18,19] Also, NIR-emitting (700−1500 nm) MNCs are considered suitable candidates for the biological applications.[20,21] However, preparing water-soluble MNCs with all these desirable properties is still a challenge.[22,23]

CuNCs have gained profound interest in recent years due to their cost-effectiveness, along with the distinct properties of copper compared to gold and silver counterparts.[24−26] However, CuNCs are much less explored mainly because of the low redox potential of copper, which makes them difficult to stabilize and also limits their structural characterization through the SC-XRD technique.[27−33]

There are various challenges associated with the processes involving crystal growth and analysis of MNCs, including heterogeneity, weak intercluster interactions, and inherent flexibility of the ligand shell, which hinder the long-range order in MNCs.[34−37] Despite these challenges, a range of successful attempts have reported high-quality single crystals of noble MNCs.[37−39] In contrast, the crystallization of CuNCs continues to pose significant difficulties, largely due to their high sensitivity to air and oxidative degradation.[40] To mitigate these shortcomings, developing MNCs as catalysts has emerged as another breakthrough in nanocluster chemistry.[5,6,41] The nanoclusters offer an excellent platform for catalytic activity because of the availability of a large specific surface area, unique electronic structures, and accessible active sites.[5]

Received: May 3, 2026
Revised: June 5, 2026
Accepted: June 9, 2026

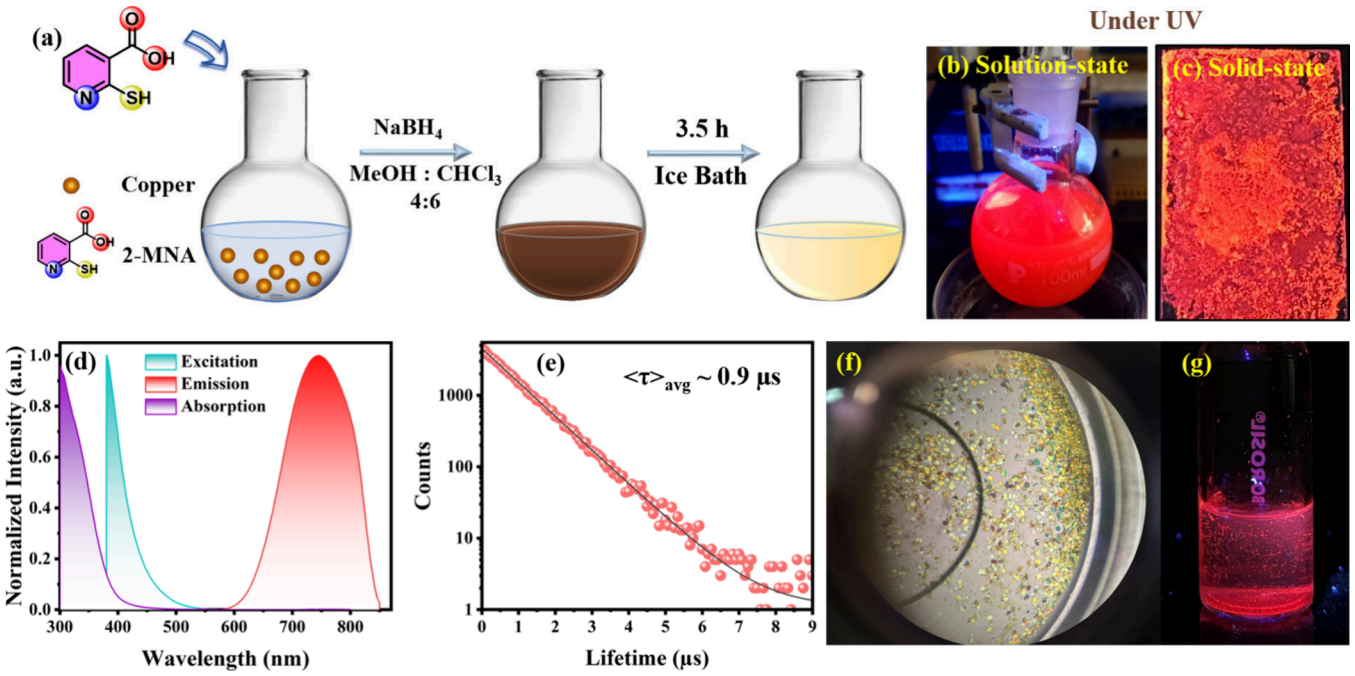

Figure 1. (a) Schematic representation of the preparation of 2-MNA-templated CuNCs. Photographic image of the CuNCs (b) prepared in bulk and (c) in the solid-state, under UV light. (d) Absorption, excitation, and emission spectra (λ_{ex} ~ 380 nm, λ_{em} = 745 nm) of the CuNCs in water displaying a large Stokes shift of 365 nm. (e) The lifetime decay plot of the CuNCs in water. The photographic image of the as-obtained crystals of the CuNCs displaying a well-defined block-shaped morphology acquired by the CuNCs under (f) ambient light, and (g) UV light, displaying an intense red emission in the crystalline form.

Metal nanoparticles (primarily Au and Ag) have been reported so far for the catalytic reduction of organic dyes.[42,43] However, they suffer from aggregation and agglomeration, limiting their practical usage.[44] CuNCs offer an environmentally friendly and cost-effective alternative in this regard. However, their application is limited by the challenges associated with their synthesis and stability.[45,46] Notably, the distinct Fermi level of Cu compared to Ag and Au makes them promising candidates for undergoing the catalytic reduction process, as the energy difference between the highest occupied molecular orbital (HOMO) and lowest unoccupied molecular orbital (LUMO) is determined by the Fermi level.[47] Additionally, many target dyes have a band gap similar to CuNCs, supporting their effectiveness for such applications.[48]

Herein, we have prepared 2-mercaptonicotinic acid (MNA) templated CuNCs that display intense red emission in solution and the solid state, and were water-soluble due to the presence of a polar carboxylate moiety in the MNA ligand (Figure 1a).[49] The ΔE_{ST} values were quantified through experimental and theoretical calculations, which display a highly efficient TADF mechanism. The CuNCs exhibit a significant catalytic activity for the reduction of ferricyanide to ferrocyanide, which was chosen as a model reaction.[50] Moreover, the efficient catalytic reduction of an organic dye (Methylene Blue) also corroborates the catalytic behavior of CuNCs in reduction reactions.

The optimized conditions for the preparation of 2-mercaptonicotinic acid (2-MNA) templated CuNCs, and the associated control experiments for obtaining the maximum PL intensity have been summarized in Figure S1 (please refer to Supporting Information for experimental details).[49] The optimized reaction scheme is depicted in Figure 1a. It should be noted that the synthetic protocol was scalable even up to 10 times the optimized reaction conditions, enabling the bulk synthesis of the CuNCs (Figure 1b). The photoluminescence spectra in solid-state for the CuNCs had a striking resemblance to that observed in the mixed solvent system (Figure S2a and Figure 1c), depicting the rigid nature of the CuNCs.[49] In the absorption spectra (Figure S2b), a well-defined absorption peak centered at ~365 nm indicated the formation of highly homogeneous nanoclusters with a known composition.[51,52] Moreover, the Surface Plasmon Resonance (SPR) band, which generally appears at around 550−650 nm for copper nanoparticles, was completely absent in the system (Figure S2b).[52] The CuNCs display a broad excitation spectrum with the maxima centered at ~370 nm, which is also in agreement with the broad absorption band observed for the CuNCs (Figure S2c). The CuNCs display intense red emission with the maxima centered at 680 nm, when excited at 380 nm (Figure S2c). A huge Stokes shift of 310 nm, depicted the involvement of triplet states behind the emission mechanism.[49]

The CuNCs display significantly high photostability (Figure S2d), along with the large Stokes shift, which is ideal for various applications of nanoclusters in materials science. The excitation and emission maxima for the CuNCs prepared in bulk are centered at ~370 nm and ~685 nm, respectively (Figure S3). The negligible change in the excitation and emission maxima confirmed that the nanoclusters have similar composition and photophysical features, even when prepared in bulk (10× scale). Incorporation of a highly polar carboxylate group on the surface of the MNCs opens up the opportunity of tuning the emission maxima of CuNCs in various solvent environments (Figure S4a).[53] The CuNCs show a comparatively red-shifted emission maxima in polar protic solvents like ethanol, methanol, and water. The maximum red-shift was observed for CuNCs in water with an emission maximum centered at ~ 745 nm. More importantly, we observed that the CuNCs were highly water-soluble due to the presence of a

https://doi.org/10.1021/acs.jpclett.6c01437
J. Phys. Chem. Lett. XXXX, XXX, XXX−XXX

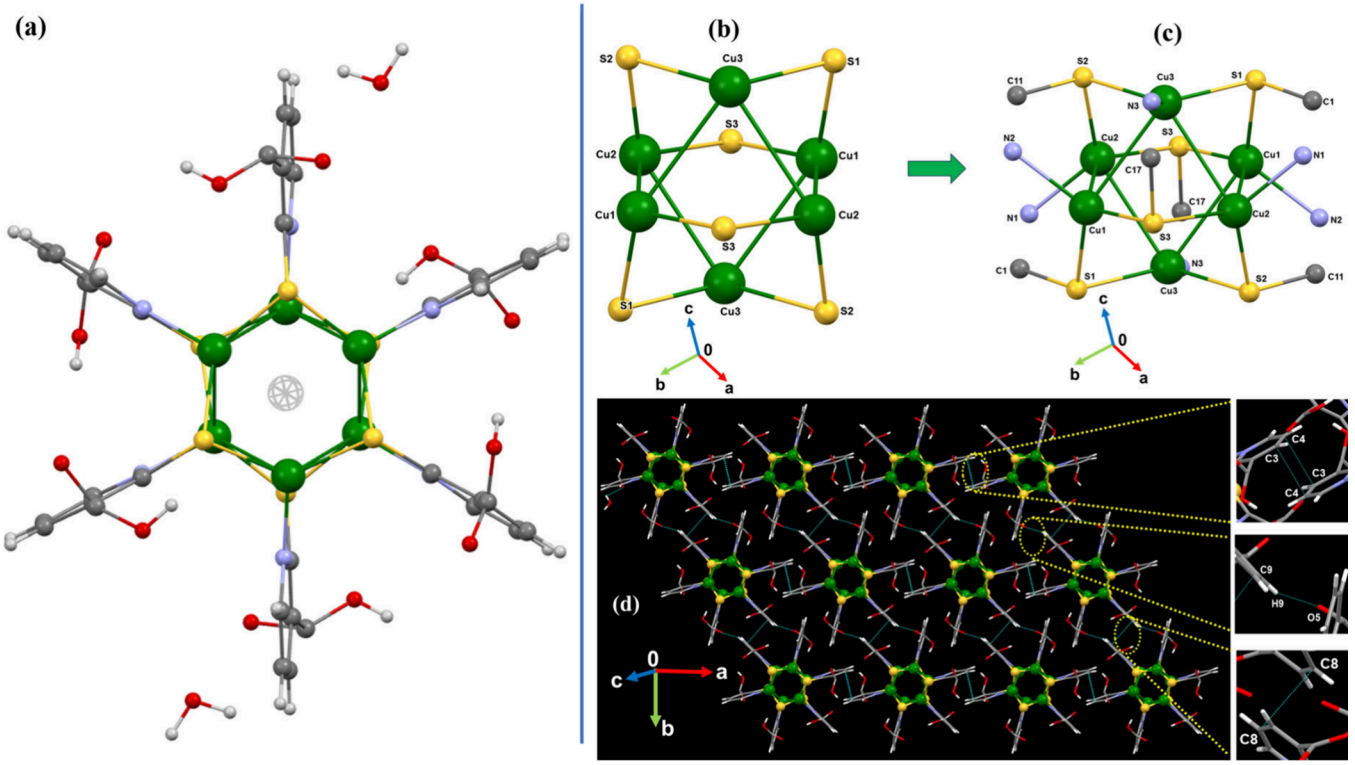

Figure 2. (a) Dimer formation via the center of inversion, shown as the central hollow gray sphere. The green, yellow, red, violet, dark gray, and light gray spheres indicate the copper, sulfur, oxygen, nitrogen, carbon, and hydrogen atoms, respectively. (b, c) Central core and its ligand connectivity in the nanocluster. (d) Crystal packing of Cu_6 in the *ab*-plane showing $\pi\cdots\pi$ interactions.

highly polar carboxylate group on the surface of the CuNCs. Therefore, to enhance the applicability of our nanoclusters, considering their broader scope in catalysis and biological applications, we conducted further studies in water.

The absorption, excitation, and emission spectra of the CuNCs dissolved in water are displayed in Figure 1d. The CuNCs exhibit an emission maximum centered at 745 nm with an excitation maximum centered at around ∼ 380 nm in water. Moreover, the CuNCs show an unaltered emission maxima with excitation wavelength as depicted in their excitation-dependent emission spectra (Figure S4b). The nonvariant emission maxima as a function of the excitation wavelength depict the homogeneous nature of the CuNCs, and also the fixed HOMO−LUMO gap for the CuNCs.[54] The CuNCs exhibit a long excited-state lifetime of ∼0.9 μs (excitation source: a 355 nm SpectraLED), depicting the triplet nature of the excited state (Figure 1e). Moreover, the long lifetime with a large Stokes shift also represents a more prominent involvement of charge transfer between the metal and ligand (LMCT) and/or ligand-to-metal−metal charge transfer (LMMCT) compared to interband and intraband transitions.[26,55] In this phenomenon, the electrons are transferred between metal and ligand, followed by radiative relaxation via a metal-centered triplet state, resulting in a red-shifted emission maxima for the MNCs. The involvement of the charge transfer phenomenon behind the emission mechanism of MNCs was further confirmed by using methyl viologen dichloride hydrate (MV^{2+}), a well-known electron scavenger (Figure S5) known for its property to disrupt the CT within the NCs, resulting in the quenching of the PL intensity.[56]

Transmission Electron Microscopy (TEM) images, as shown in Figure S6a, display a significantly high homogeneous size distribution of the CuNCs with an average diameter of 1.74 ± 0.28 nm (Figure S6b). Additionally, the CuNCs were present in the aggregated form in the mixed-solvent system (Figure S6a). However, when observed in water, discrete morphology for the CuNCs was observed (Figure S7). Thus, the CuNCs display aggregation-induced blue-shifted emission as evident from their photoluminescence profiles and the microscopy data.[57] In the Fourier Transform Infrared (FTIR) data (Figure S8), we observed that both the peaks corresponding to S−H and N−H stretching frequency at 2200 cm^{-1} and 2800 cm^{-1}, respectively (upper panel), are completely lost upon the formation of the nanoclusters (lower panel).[58] This suggests that both nitrogen and sulfur atoms of the ligand are involved in the binding with the copper core (Figure S8). Thereafter, the ESI-MS analysis (in negative-ion mode) was performed to estimate the possible composition of the nanoclusters (Figure S9). It should be noted that in the isotopic patterns corresponding to every peak observed in ESI-MS data, the separation of m/z value of 1 unit depicted the overall charge of −1 over the detected entity.[59] The chemical composition corresponding to the most intense peak present at 1149.6 m/z was estimated to be $[Cu_6(MNA\text{-}H)_5\text{-}3H]^-$. The simulated isotopic pattern corresponding to the above composition was in excellent agreement with the experimental isotopic pattern (inset of Figure S9). The subsequent peaks at m/z 1171.4, 1193.5, and 1215.5 are equidistant from each other, with an m/z difference of ∼22. This is attributed to the subsequent substitution of 1 H^+ with 1 sodium ion (Na^+) in the −COOH group present on the surface ligands of the CuNCs.

Further, for clear structural information, we crystallized CuNCs through the vapor diffusion technique,[30] and the

https://doi.org/10.1021/acs.jpclett.6c01437
J. Phys. Chem. Lett. XXXX, XXX, XXX−XXX

crystals so obtained were captured under the optical microscope (Figure 1f). The crystals displayed intense red emission under UV light, as shown in the photographic image (Figure 1g).

The SC-XRD analysis of the CuNC crystals was performed to gain insight into the structure of the nanoclusters. Tiny block crystals of the copper nanocluster were obtained from a mixture of methanol/THF using the vapor diffusion technique at room temperature (see methods in the Supporting Information for more details). Further, these crystals were utilized to perform single-crystal X-ray diffraction experiments (Figure S10, Table S1), to determine the 3D atomic connectivity. The molecule crystallizes in the monoclinic centrosymmetric $C2/c$ space group with half a molecule in the asymmetric unit and the other half being generated via the center of inversion (Figure 2a). In addition to the nanocluster, water molecules are trapped in the crystal lattice. The central core of the nanocluster consists of Cu−Cu and Cu−S bonds (Figure 2b). Each Cu atom forms two Cu−Cu bonds and two Cu−S bonds, while each sulfur atom forms two S−Cu bonds within the central core (Figure 2b). Figure 2c shows the ligand connectivity with the central core, where each Cu forms a Cu−N bond (a total of 6 Cu−N bonds), and each sulfur forms an S−C bond (a total of 6 S−C bonds). Overall, each Cu atom adopts a square pyramidal geometry. The bond distances are summarized in Table 1 based on Figure 2c. The crystal packing

Table 1. Relevant Bond Distances of Cu6-nanocluster

Bond[a]	Distance (Å)
Cu1−Cu2	2.8323(3)
Cu1−Cu3[b] (−x + 1, −y + 1, −z + 1)	2.8160(4)
Cu2−Cu3	2.7899(3)
Cu1−S1/Cu1−S3[b] (−x + 1, −y + 1, −z + 1)	2.2586(3)/2.2221(3)
Cu2−S2/Cu2−S3	2.2271(2)/2.2413(2)
Cu3−S1/Cu3−S2[b] (−x + 1, −y + 1, −z + 1)	2.2259(2)/2.2425(3)
Cu1−N2/S1−C1	2.0047(2)/1.7179(2)
Cu2−N1/S2−C11	1.9865(2)/1.7341(2)
Cu3−N3/S3−C17	2.0157(3)/1.7465(2)

[a]Uncorrected distances from PARST. [b]Intermolecular contacts.

of the molecule is mainly stabilized through $\pi\cdots\pi$ interactions that form a 2D sheet in the ab-plane (Figure 2d). Along the a-axis, the molecule creates a 1D chain using the centrosymmetric dimer (C3) $\pi\cdots\pi$ (C4) interaction. This chain is further linked by (C8) $\pi\cdots\pi$ (C8) interactions and C9−H9···O5 dimer along the b-axis (Figure 2d, Table 2). Further, we verified the phase purity of the bulk sample by performing the Powder X-ray Diffraction (PXRD) data analysis. The experimentally obtained PXRD spectra overlapped well with the simulated PXRD spectra generated from the single-crystal XRD data

Table 2. List of intermolecular interactions for Cu6-nanocluster

Interactions	Symmetry code	D···A (Å)	H···A (Å)	D−H···A (deg)
(C3) $\pi\cdots\pi$ (C4)	$-x, -y + 1, -z + 1$	3.2477(4)		
(C8) $\pi\cdots\pi$ (C8)	$-x + 1/2, -y + 1/2, -z + 1$	3.3285(4)		
C9−H9···O5[a]	$x + 1/2, +y + 1/2, +z$	3.7000(4)	2.74	148

[a]Neutron normalized distance.

(Figure S11). This analysis further confirmed that the single-crystal structure ($Cu_6(MNA)_6$) is a representative of the bulk sample. Moreover, the apparent discrepancy between the composition determined from ESI-MS analysis and the crystal structure may be attributed to partial ligand dissociation, which can occur during the ionization and desolvation processes in ESI-MS.[60]

The pronounced red emission of the CuNCs, coupled with a long excited-state lifetime (~0.9 μs), prompted investigation of the triplet-state involvement in the emission mechanism. The Time Resolved Emission Spectroscopy (TRES) data at a 0.9 μs time delay strongly overlapped with the steady state emission spectra (Figure 3a), indicating the emission originates from the same emissive excited-state, which suggests that the phenomenon of delayed fluorescence may be operational, and hence we have studied the same in detail.[49,61] Further, the temperature-dependent measurements (Figure 3b) reveal an enhancement in the photoluminescence intensity upon increasing the temperature from 283 to 308 K, followed by a decline up to 323 K. This enhancement is also accompanied by a blue shift in the emission maxima (Figure S12) from ~ 750 nm (283 K) to ~ 735 nm (323 K). This observation supported the TADF mechanism.[62] At higher temperatures, reverse intersystem crossing (rISC) results in the transition from the lowest excited triplet state (T_1) to the first excited singlet state (S_1), followed by a radiative transition to the ground state (S_0), which results in delayed fluorescence. Upon increasing temperature, the T_1 to S_1 transitions enhance, generating a blue-shift in the emission maxima. The curve obtained from the PL intensity against temperature plot (please refer to Figure 3b) illustrates that S_1 and T_1 are in equilibrium with each other (Figure S13, upper panel).[62] Upon increasing the temperature, the rISC enhances, resulting in greater PL intensity. However, after a certain temperature, further increments result in thermal depopulation of the excited state, resulting in the subsequent decrement in the emission intensity.[62] Further, we monitored integrated PL intensity as a function of temperature (Figure S13 lower panel) and observed a similar trend as obtained in PL intensity, as depicted in Figure S13, upper panel. The increase in the integrated PL intensity (not just the apparent peak) upon increasing temperature further supports the TADF mechanism operational in the system. For an efficient TADF process, ΔE_{ST} should be sufficiently small to facilitate the rISC, which was further verified by temperature-dependent excited-state lifetime measurements (Figure 3c).[14] Upon increasing the temperature from 283 to 323 K, the lifetime decreased from 1.06 to 0.64 μs (Table S2). The temperature vs average lifetime data was fitted with the following Boltzmann's eq (eq 1) derived from the TADF model (Figure 3d and Table S3):[62,63]

$$\tau = \frac{3 + \exp\left(\frac{-\Delta E(S_1 - T_1)}{k_B T}\right)}{\left(\frac{3}{\tau(T_1)}\right) + \frac{1}{\tau(S_1) \times \exp\left(\frac{\Delta E(S_1 - T_1)}{k_B T}\right)}} \quad (1)$$

Here τ, $\tau(S_1)$, and $\tau(T_1)$ represent the average lifetime, lifetime of the singlet state, and lifetime of the triplet state, respectively; k_B is the Boltzmann constant, T is the temperature in kelvin, and $\Delta E(S_1-T_1)$ is the energy difference between the excited singlet and triplet state energy levels. For

https://doi.org/10.1021/acs.jpclett.6c01437
J. Phys. Chem. Lett. XXXX, XXX, XXX−XXX

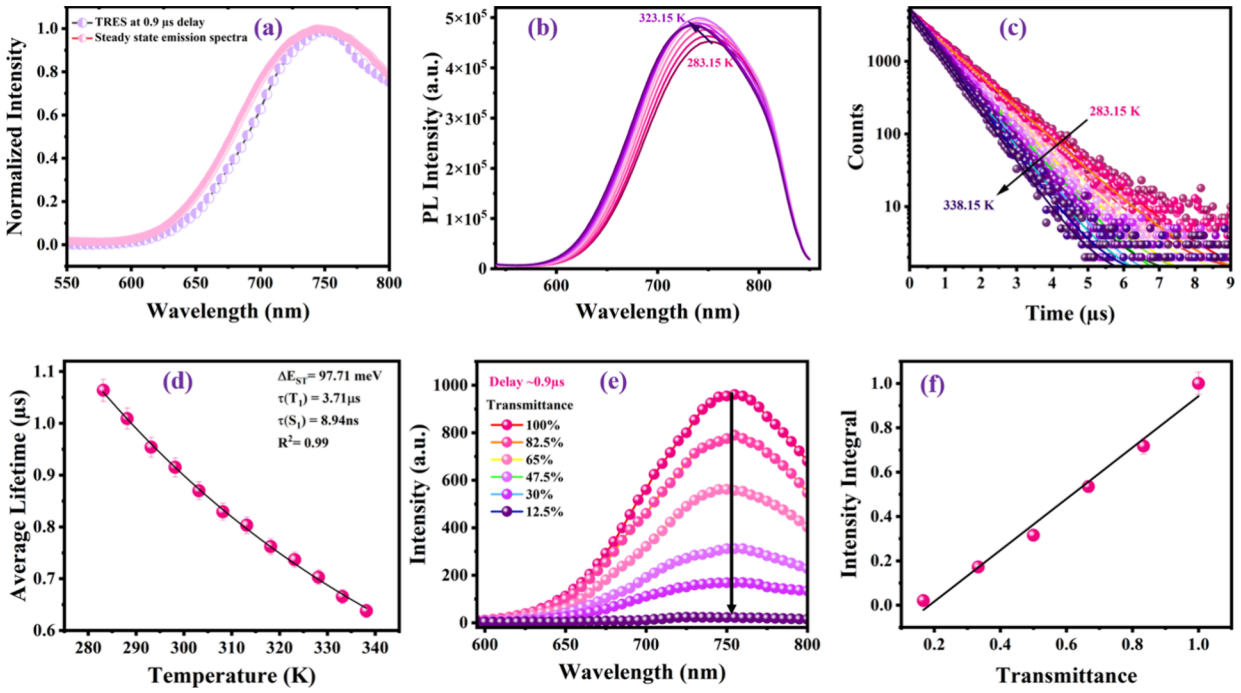

Figure 3. (a) TRES at 0.9 μs time delay overlapping well with the steady-state emission spectra of the CuNCs. (b) Temperature-dependent photoluminescence spectra of the CuNCs depict the increment in the photoluminescence intensity upon increasing temperature. (c) The temperature-dependent lifetime decay plots of the CuNCs depict a decrease in the lifetime with an increase in temperature. (d) Plot of the average lifetime vs temperature data fitting using the TADF model. (e) Photoluminescence intensity at varying excitation transmittance, the data were collected at a 0.9 μs time delay. (f) Plot of the excitation transmittance vs intensity integral depicting a linear relationship (slope ~ 1.16) between the two.

an efficient TADF process, the $\Delta E(S_1-T_1)$ value should be less than 3000 cm^{-1} or 370 meV.[63]

For the CuNCs, upon fitting the temperature vs lifetime data through eq 1, the parameters obtained are as follows: $\Delta E(S_1-T_1) \sim 788\ cm^{-1}$ (=97.7 meV), $\tau(T_1)$ and $\tau(S_1)$ were 3.71 μs and 8.94 ns, respectively (Table S3). The above values suggest a highly efficient TADF process operational in the system. TADF materials can be categorized into two types based on the rate of intersystem crossing.[16] First, the materials having the rate of ISC typically within the range of $10^5-10^8\ s^{-1}$, e.g., organic TADF materials, diborane compounds, etc. These materials generally exhibit a biexponential lifetime decay profile, clearly distinguishing prompt fluorescence (short-lived component) and TADF (long-lived component).[16] Other category comprises materials having the rate of ISC within $10^8-10^{11}\ s^{-1}$. In this case, a pre-equilibrium is established between S_1 and T_1 before the emission.[16] Consequently, the photoluminescence decay curves follow the monoexponential behavior in the microsecond scale as seen in metal carbene complexes.[16] Thus, for the CuNCs, we can assign the monoexponential behavior of the decay curves to the very fast ISC process, making the prompt fluorescence component instrumentally unresolved. Additionally, to examine the nature of the emissive excited-state, we performed emission wavelength-dependent fluorescence lifetime measurements. Interestingly, the measured decay lifetimes remained essentially unchanged across the monitored emission wavelengths (Figure S14, Table S4). This observation suggests that the delayed emission originates predominantly from a single emissive excited state rather than from multiple independently emitting states that exhibit distinct decay dynamics. This behavior is consistent with delayed fluorescence arising from thermally activated reverse intersystem crossing (*rISC*), and supports a common emission origin for prompt fluorescence and TADF.

Moreover, upon cooling, the emission spectra exhibited a noticeable blue shift (from 745 nm at ~293 K to 680 nm at ~77 K) attributed to suppression of structural relaxation in the excited state and reduced stabilization of the charge-transfer excited state.[64] The restricted geometrical distortion due to suppression in intramolecular rotation and vibration of surface ligands at low temperature results in emission from a less-relaxed higher-energy excited state, which is further supported by the observation of a long lifetime of ~29.02 μs at ~77 K (Figure S15 and Table S5). Additionally, the new peak observed at ~525 nm is attributed to the higher-energy state emitting radiatively exclusively at low temperature.[65] Also, the photoluminescence and lifetime decay were collected under inert conditions, i.e., in the absence of oxygen (Figure S16, Table S6). The nonvariant nature of the steady-state and time-resolved spectroscopic signatures reveals that the as-prepared CuNCs are insensitive to the presence of oxygen.[66] Further, to distinguish the TADF mechanism from any other delayed fluorescence processes possible in the system, excitation-transmittance-dependent TRES intensity measurements were carried out.[67] The time-resolved emission spectra were taken at varying excitation transmittance controlled by an iris. As depicted in Figure 3e, the TRES intensity at 0.9 μs time delay decreases with a decrease in the excitation transmittance. The linear dependence of the TRES intensity on the transmittance of the excitation source (slope ~ 1.1, Figure 3f) corroborated the purely thermally activated nature of the delayed fluorescence, and no other higher-order excitonic phenomenon is involved.[67] Therefore, all the above experiments establish a

https://doi.org/10.1021/acs.jpclett.6c01437
J. Phys. Chem. Lett. XXXX, XXX, XXX−XXX

highly efficient TADF mechanism functional in CuNCs, which has been well-supported by a theoretical approach as discussed below.

The molecular model considered to understand the TADF mechanism is depicted in Figure 4a. The HOMO and LUMO

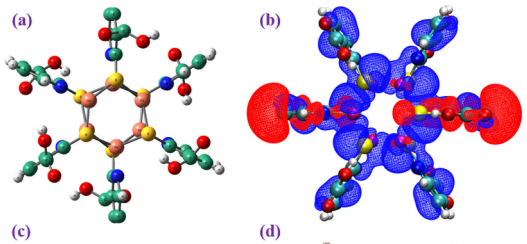

Solvent	Water
ΔE_{ST} (eV)	0.20
f	0.001
H_{SO} (cm^{-1})	3.29
k_{PF} (s^{-1})	2.03×10^{5}
k_{rISC} (s^{-1})	9.09×10^{5}
K_{ISC} (s^{-1})	6.22×10^{9}
k_{DF} (s^{-1})	1.66×10^{5}

Figure 4. (a) The molecular model used in the calculation, with pink, yellow, red, blue, green, white representing copper, sulfur, oxygen, nitrogen, carbon, and hydrogen, respectively. (b) The HOMO (blue) and LUMO (red) of the molecular system made with VMD, with isovalue 0.01. (c) Calculated photophysical parameters of the studied system, including oscillator strength, singlet−triplet energy gap, spin−orbit coupling, and excited-state rate constants relevant to TADF behavior. (d) Charge transfer characteristics of the investigated system. The charge transfer direction is from pink lobes (+) to yellow lobes (−).

distributions are illustrated in Figure 4b. The HOMO (blue lobes) is mainly localized on the copper and sulfur atoms of the nanocluster, while the LUMO (red lobes) is primarily localized on the oxygen atoms of the phenyl rings on opposite sides. A key observation is that the HOMO and LUMO do not overlap significantly in space (at most of the places). Wherever a blue lobe (HOMO) is present, the probability of finding a red lobe (LUMO) on the same atom is very low. This clear spatial separation implies that the HOMO and LUMO are well isolated, leading to minimal orbital interaction and, consequently, a small singlet−triplet energy gap (ΔE_{ST}), as evident from our experimental observations. Such an arrangement satisfies one of the fundamental conditions for a molecule to exhibit TADF, namely, minimal HOMO−LUMO overlap, which enhances the efficiency of reverse intersystem crossing (*r*ISC).

The photophysical parameters of the nanocluster were further calculated (Figure 4c, see Supporting Information for details): the first singlet excited-state energy (E_{S1}) is 2.165 eV.[68,69] The estimated singlet−triplet gap (ΔE_{ST}) is 0.20 eV, whereas the experimental value is approximately 0.10 eV. Given the small magnitude of this parameter, such agreement is quite reasonable. The oscillator strength (f), which reflects the probability of radiative emission, is relatively low (∼0.001). The prompt fluorescence rate (k_{PF}) is on the order of 10^5 s^{-1}, while the intersystem crossing (k_{ISC}) and reverse intersystem crossing (k_{rISC}) rates are approximately 10^9 s^{-1} and 10^5 s^{-1}, respectively. The delayed fluorescence rate (k_{DF}) arises from the combined contributions of k_{PF} and k_{rISC}, therefore lies in the range of 10^5 s^{-1}. The spin−orbit coupling (H_{SO}) quantifies the extent of singlet−triplet mixing and directly governs both the ISC and *r*ISC processes. The observed magnitudes of H_{SO}, together with the small singlet−triplet energy gap (ΔE_{ST}), are consistent with TADF behavior. These parameters facilitate an efficient *r*ISC process with a rate comparable to the prompt fluorescence rate, resulting in delayed fluorescence on the order of 10^5 s^{-1}. Further, analytical calculation of singlet exciton density decay profiles using the three-state (S_0, S_1, T_1) kinetic model yielded a macroscopic delayed decay lifetime ($\tau_{delayed} = -1/\lambda_1$) of ≈18.80 μs (1.88×10^{-5} s), Figure S17 (please see Supporting Information for further details).[70,71] Overall, the system can be classified as TADF-active. However, the relatively low oscillator strength, which directly impacts the radiative emission probability, along with the comparatively high intersystem crossing rate, may limit the overall emission efficiency or quantum yield. This was further supported by the relatively low photoluminescence quantum yield of ∼ 0.1% for the CuNCs in water (using Coumarin 102 as a standard reference), and low absolute photoluminescence quantum yield of ∼0.5% in solid-state (aggregated form), observed experimentally (Figure S18). We further calculated the radiative decay rate (k_r) and nonradiative decay rate (k_{nr}) through experimentally determined relative photoluminescence quantum yield ($\Phi \sim 0.1\%$) and average excited-state lifetime ($\tau \sim 0.9$ μs) in water. The radiative decay rate (k_r) and nonradiative decay rate (k_{nr}) were calculated to be $\sim 1.1 \times 10^3$ s^{-1} and 1.1×10^6 s^{-1}, respectively.

After calculating the photophysical parameters, we also determined the charge-transfer (CT) number of the investigated system (Figure 4d). This parameter describes the charge-transfer within the system quantitatively and ranges from 0 to 1. The Q_{CT} value (0.894) is approaching 1, indicating that long-range charge-transfer is operative here. The accompanying charge-transfer density map illustrates this process, showing that upon excitation from the ground to the excited-state, electron density migrates from the ligands to the metal regions (Figure 4d). The yellow central region represents the negative (electron) domain, while the outer regions represent the accumulation of positive charge, indicating the direction of charge transfer within the molecule. Overall, the results reveal that the $Cu_6(MNA)_6$ nanocluster exhibits pronounced ligand-to-metal charge-transfer characteristics, a strong spatial separation between the HOMO and LUMO, and a small ΔE_{ST}, collectively confirming its potential for TADF.

Noble MNCs (AuNCs and AgNCs) have been studied so far as catalysts for a variety of reactions, due to their high surface-to-volume ratio.[5] However, a demand for the less expensive and efficient alternative intrigued us to test the catalytic activity of the CuNCs. Catalytic activity of such a small 6-atom CuNC is scarcely reported. Therefore, we first checked the catalytic activity of the CuNCs for a 1-electron reduction reaction for which we chose the ferricyanide to ferrocyanide conversion as our model reaction (eq 2).[50]

$$2S_2O_3^{2-} + 2[Fe(CN)_6]^{3-} \rightarrow S_4O_6^{2-} + 2[Fe(CN)_6]^{4-} \quad (2)$$

The reduction of ferricyanide was carried out using thiosulfate as a reducing agent in an aqueous medium at 25 °C. The depletion in the absorption peak at 420 nm, corresponding to the ferricyanide, was monitored as a function of time for the determination of the rate constant.[50] Upon using 1 mol % CuNCs with respect to the concentration of

https://doi.org/10.1021/acs.jpclett.6c01437
J. Phys. Chem. Lett. XXXX, XXX, XXX−XXX

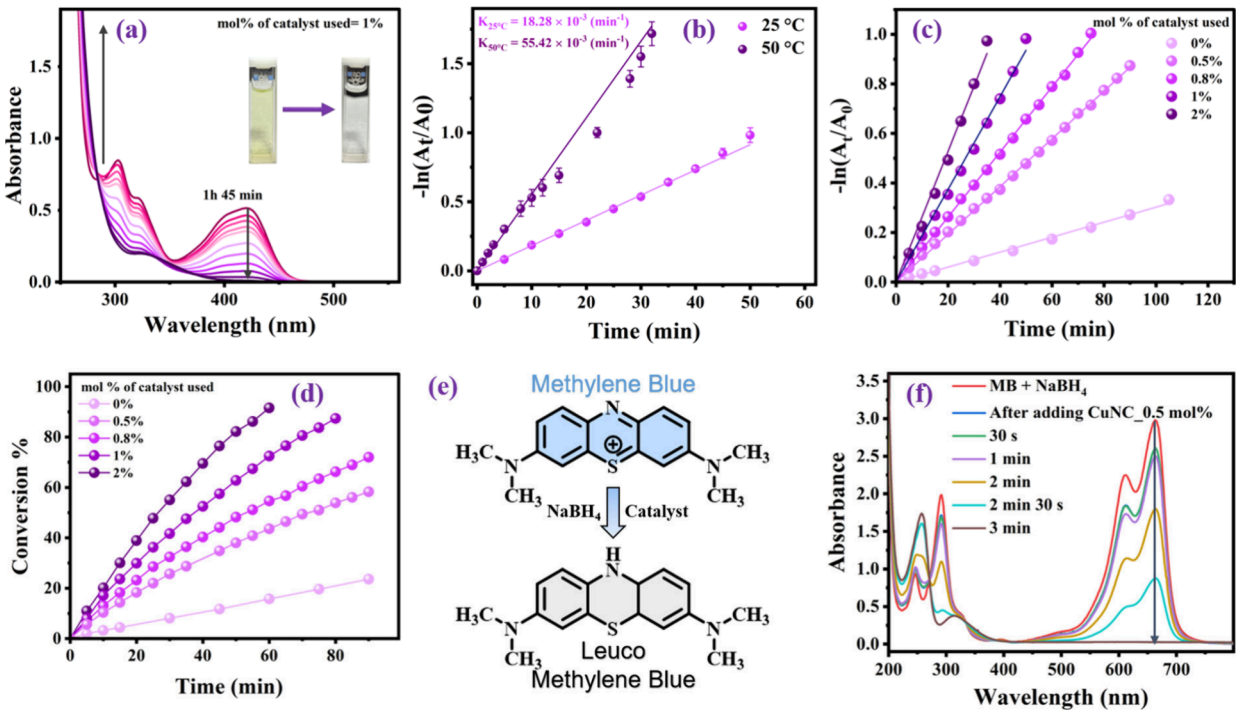

Figure 5. (a) The time-dependent absorption spectra depicting the catalytic reduction of potassium ferricyanide using 1 mol% of the Catalyst with respect to the concentration of the $K_3Fe(CN)_6$. (b) The kinetic analysis of the reduction process at different temperatures, the error bars were determined based on three independent experiments. (c) The kinetic analysis of the reduction process at different amounts of the catalyst used, and (d) the percentage conversion. (e) The schematic representation of the catalytic reduction of Methylene Blue (MB) to Leuco Methylene Blue (LMB) in the presence of a reducing agent ($NaBH_4$) and the catalyst. (f) The catalytic reduction of MB upon using 0.5 mol % catalyst with respect to the molar concentration of the substrate (MB).

ferricyanide used Figure 5a, the reduction reaction proceeds with a successive decrement in the absorption band at ∼420 nm, which gets completely attenuated after 1 h 45 min. The decrease in the absorption band is also accompanied by a color change from yellow to transparent solution (inset of Figure 5a). Simultaneously, an increment in the absorbance at ∼240 nm was observed, corroborating the conversion of ferricyanide to ferrocyanide (Figure 5a).[72] The presence of a well-defined isosbestic point at ∼265 nm dictates that the conversion is stoichiometric in nature.[72−74] Moreover, it also suggests that no intermediate specie(s) are involved in the reaction. In the absence of the catalyst, a very small change in the absorption peak was observed (Figure S19a), clearly representing the catalytic behavior of the CuNCs. Further, a nonvariant nature of the absorption spectra of the ferricyanide (monitored at 420 nm) in the absence of a reducing agent ($Na_2S_2O_3$) suggested the exclusive role of the CuNCs as a catalyst (Figure S19b). Considering the pseudo-first-order kinetics for the reaction, rate constants were calculated by the slope of $-\ln(A_t/A_0)$ vs time plot, as depicted in Figure 5b, and Table S7 (see SI for further details). The rate constant for the catalytic reduction reaction upon adding only 1 mol % of the catalyst was calculated to be 18.71×10^{-3} min^{-1} at 25 °C (Table S7). The reaction rate constants can be further increased upon increasing the reaction temperature (Figure 5b). The rate constant for the same reaction was calculated to be 55.42×10^{-3} min^{-1} at 50 °C (Figure 5b and Table S7).

Moreover, we optimized the catalyst concentration for the efficient conversion; the rate constants increased with an increase in the amount of catalyst (Figure 5c, Table S7). The rate constant for the uncatalyzed reaction was calculated to be 2.87×10^{-3} min^{-1} at 25 °C (Figure 5b, Table S7). Therefore, using only 1 mol % of the catalyst led to ∼6 times enhancement in the rate compared to the uncatalyzed reaction. The percentage conversion of ferricyanide to ferrocyanide over time using different amounts of catalyst is presented in Figure 5d. Further, we verified the formation of ferrocyanide through a Prussian Blue test (Figure S20).[74] Additionally, no color change was observed upon adding ferric chloride to the solution of ferricyanide, suggesting that the substrate was free from ferrocyanide. Thus, all the above experimental results conclude the efficient conversion of ferricyanide to ferrocyanide upon using the CuNCs as a catalyst.

Catalyzing the reduction reaction of organic water pollutants has emerged as a cost and energy-efficient wastewater treatment technique. Methylene Blue (MB) is commonly used as a coloring agent in the textile and paint industries.[75] It is discharged from the industries at very high levels into the water bodies, which is threatening the environment. The reduction of MB converts it to a less toxic form, known as Leuco Methylene Blue (Figure 5e).[75] The process of efficient reduction of this dye requires the presence of a catalyst. Moreover, the catalysts are preferred to be prepared in an eco-friendly and sustainable manner. Therefore, we explored the reduction of MB using our CuNCs.[47] Expectedly, the CuNCs display highly efficient catalytic activity for the reduction of MB (Figure 5e). On using just 0.5 mol % of the catalyst (Figure 5f), the reduction happens only within 3 min. The catalytic process was so fast that we were limited by the facilities to calculate the rate constants. Upon increasing the catalyst concentration to 0.75 mol %, reduction completes within 90 s (Figure 5f and Figure S21a). Surprisingly, on using

https://doi.org/10.1021/acs.jpclett.6c01437
J. Phys. Chem. Lett. XXXX, XXX, XXX−XXX

a catalyst concentration of 1 mol %, the reduction happens almost immediately (Figure S21b). Also, no change in the absorbance corresponding to MB was observed even after 2h without the catalyst, corroborating highly efficient catalytic activity for the CuNCs (Figure S21c).

The present kind of reduction catalysis is rarely reported for the nonhydride CuNCs, a comparative study of the catalytic rate constants for the reduction reactions using metal-based systems is presented in Table S8.[45,76−78] Therefore, to gain insight into the mechanism of the catalytic reduction, we further screened a variety of substrates having different coordination sites. The CuNCs do not catalyze the reduction of Congo Red (an anionic dye), Rhodamine B, and Nile Blue (cationic dyes, Figure S22). Instead, in the case of Nile Blue, a retardation in the rate of the reaction was observed. Nile Blue has an excellent structural correlation with MB. However, it contains a central oxazine ring in place of the thiazine ring. Thus, this may be attributed to the soft−soft interactions between the thiazine moiety and copper, which confer a stronger affinity of MB toward the CuNCs core, thereby facilitating the electron transfer processes. Hence, we substantiate that our CuNCs are also highly specific for the reduction of MB. In conclusion, red-emitting CuNCs that display intense emission in solid, solution, and crystalline states were prepared. The CuNCs are highly water-soluble and display NIR emission in an aqueous environment along with excellent solvatochromism. Red-emitting crystals of the CuNCs were structurally resolved by SC-XRD analysis, confirming composition as $Cu_6(MNA)_6$. Spectroscopic investigations reveal efficient TADF being operational in the system, supported by small ΔE_{ST} (~98 meV) and temperature-dependent measurements. Theoretical calculations also validate TADF, highlighting favorable ΔE_{ST} along with sufficient spin−orbit coupling. Additionally, the CuNCs display excellent catalytic activity for the reduction of ferricyanide and Methylene Blue, underscoring their multifaceted applicability in the aqueous phase.

■ ASSOCIATED CONTENT

Data Availability Statement

The crystal structure was deposited in the Cambridge Structural Database (CSD). The CCDC number is 2539697, and the same can be downloaded from www.ccdc.cam.ac.uk.

Supporting Information

The Supporting Information is available free of charge at https://pubs.acs.org/doi/10.1021/acs.jpclett.6c01437.

CheckCIF report (PDF)

Crystallographic data (CIF)

Experimental and characterization data (PDF)

■ AUTHOR INFORMATION

Corresponding Authors

Saptarshi Mukherjee − *Department of Chemistry, Indian Institute of Science Education and Research Bhopal, Bhopal 462 066 Madhya Pradesh, India;* orcid.org/0000-0001-8280-0754; Email: saptarshi@iiserb.ac.in

Deepak Chopra − *Department of Chemistry, Indian Institute of Science Education and Research Bhopal, Bhopal 462 066 Madhya Pradesh, India;* orcid.org/0000-0002-0018-6007; Email: dchopra@iiserb.ac.in

Anirban Mondal − *Department of Chemistry, Indian Institute of Technology Gandhinagar, Gandhinagar 382355 Gujarat, India;* orcid.org/0000-0003-3029-8840; Email: amondal@iitgn.ac.in

Authors

Sameeksha Agrawal − *Department of Chemistry, Indian Institute of Science Education and Research Bhopal, Bhopal 462 066 Madhya Pradesh, India;* orcid.org/0000-0003-1968-8223

Thrisha Swaminathan − *Department of Chemistry, Indian Institute of Science Education and Research Bhopal, Bhopal 462 066 Madhya Pradesh, India*

Sanyam − *Department of Chemistry, Indian Institute of Technology Gandhinagar, Gandhinagar 382355 Gujarat, India;* orcid.org/0000-0001-7410-8207

Koushik Mandal − *Department of Chemistry, Indian Institute of Science Education and Research Bhopal, Bhopal 462 066 Madhya Pradesh, India*

Complete contact information is available at: https://pubs.acs.org/10.1021/acs.jpclett.6c01437

Author Contributions

The project was conceived by S.A. and S.M. S.A. and T.S. carried out the experiments. S.A., T.S., and S.M. analyzed the data. Sanyam carried out the theoretical investigations with inputs from A.M. K.M. carried out the SC-XRD studies with inputs from D.C. All the authors contributed to writing the manuscript.

Notes

The authors declare no competing financial interest.

■ ACKNOWLEDGMENTS

S.A. thanks IISER Bhopal for providing a fellowship. S.M. thanks SERB-ANRF, Govt. of India (Project No: SERB-CRG/2023/000473) for financial assistance. The authors also thank IISER Bhopal for providing the necessary research infrastructure. Sanyam and A.M. acknowledge IIT Gandhinagar and PARAM Ananta for providing computational resources. We also acknowledge the FIST Facility for TEM, Department of Chemistry, and the SC-XRD facility of the CIF, IISER Bhopal.

■ REFERENCES

(1) Yang, G.; Wang, Z.; Du, F.; Jiang, F.; Yuan, X.; Ying, J. Y. Ultrasmall Coinage Metal Nanoclusters as Promising Theranostic Probes for Biomedical Applications. *J. Am. Chem. Soc.* **2023**, *145* (22), 11879−11898.

(2) Nasrollahpour, H.; Sánchez, B. J.; Sillanpää, M.; Moradi, R. Metal Nanoclusters in Point-of-Care Sensing and Biosensing Applications. *ACS Appl. Nano Mater.* **2023**, *6* (14), 12609−12672.

(3) Lin, H.; Song, X.; Chai, O. J. H.; Yao, Q.; Yang, H.; Xie, J. Photoluminescent Characterization of Metal Nanoclusters: Basic Parameters, Methods, and Applications. *Adv. Mater.* **2024**, *36* (25), No. e2401002.

(4) Xiao, Y.; Wu, Z.; Yao, Q.; Xie, J. Luminescent Metal Nanoclusters: Biosensing Strategies and Bioimaging Applications. *Aggregate (Hoboken)* **2021**, *2* (1), 114−132.

(5) Du, X.; Jin, R. Atomically Precise Metal Nanoclusters for Catalysis. *ACS Nano* **2019**, *13* (7), 7383−7387.

(6) Mahato, P.; Shekhar, S.; Yadav, R.; Mukherjee, S. Mechanistic Elucidation of the Catalytic Activity of Silver Nanoclusters: Exploring the Predominant Role of Electrostatic Surface. *Nanoscale* **2024**, *16* (2), 806−820.

(7) Shekhar, S.; Sarker, R.; Mahato, P.; Agrawal, S.; Mukherjee, S. pH-Switchable Phenylalanine-Templated Copper Nanoclusters: CO_2 Probing and Efficient Peroxidase Mimicking Activity. *Nanoscale* **2023**, *15* (37), 15368−15381.
(8) Lu, J.; Shao, B.; Huang, R.-W.; Gutiérrez-Arzaluz, L.; Chen, S.; Han, Z.; Yin, J.; Zhu, H.; Dayneko, S.; Hedhili, M. N.; Song, X.; Yuan, P.; Dong, C.; Zhou, R.; Saidaminov, M. I.; Zang, S.-Q.; Mohammed, O. F.; Bakr, O. M. High-Efficiency Circularly Polarized Light-Emitting Diodes Based on Chiral Metal Nanoclusters. *J. Am. Chem. Soc.* **2024**, *146* (6), 4144−4152.
(9) Zhang, D.; Zhu, M.; He, Y.; Cao, Q.; Gao, Y.; Li, H.; Lu, G.; Cui, Q.; Shen, Y.; He, H.; Dai, X.; Ye, Z. Efficient and Bright Broadband Electroluminescence Based on Environment-Friendly Metal Halide Nanoclusters. *Light Sci. Appl.* **2024**, *13* (1), 82.
(10) Zhang, S.-S.; Havenridge, S.; Zhang, C.; Wang, Z.; Feng, L.; Gao, Z.-Y.; Aikens, C. M.; Tung, C.-H.; Sun, D. Sulfide Boosting Near-Unity Photoluminescence Quantum Yield of Silver Nanocluster. *J. Am. Chem. Soc.* **2022**, *144* (40), 18305−18314.
(11) Mahato, P.; Shekhar, S.; Agrawal, S.; Pramanik, S.; Mukherjee, S. Assembly-Induced Emission in Mercaptosuccinic Acid-Templated Silver Nanoclusters: Metal Ion Selectivity and pH Sensitivity. *ACS Appl. Nano Mater.* **2022**, *5* (5), 7571−7579.
(12) Luo, L.; Liu, Z.; Mazumder, A.; Jin, R. Raising Near-Infrared Photoluminescence Quantum Yield of Au_{42} Quantum Rod to 50% in Solutions and 75% in Films. *J. Am. Chem. Soc.* **2024**, *146* (41), 27993−27997.
(13) Mitsui, M. Recent Advances in Understanding Triplet States in Metal Nanoclusters: Their Formation, Energy Transfer, and Applications in Photon Upconversion. *J. Phys. Chem. Lett.* **2024**, *15* (50), 12257−12268.
(14) Uoyama, H.; Goushi, K.; Shizu, K.; Nomura, H.; Adachi, C. Highly Efficient Organic Light-Emitting Diodes from Delayed Fluorescence. *Nature* **2012**, *492* (7428), 234−238.
(15) Akiyama, A.; Hossain, S.; Niihori, Y.; Oiwa, K.; Roy, J.; Kawawaki, T.; Pradeep, T.; Negishi, Y. Enhancement of Photoluminescence Quantum Yield of Silver Clusters by Heavy Atom Effect. *Small* **2025**, *21* (25), No. e2500700.
(16) Liu, Z.; Luo, L.; Jin, R. Visible to NIR-II Photoluminescence of Atomically Precise Gold Nanoclusters. *Adv. Mater.* **2024**, *36* (8), No. e2309073.
(17) Jiang, W.-H.; Zeng, X.-M.; Wu, M.; Qin, L.; Yao, L.-Y.; Yang, G.-Y. Thermally Activated Delayed Fluorescence-Based near-Infrared-II Luminescence and Controlled Size Growth of Silver Nanoclusters. *ACS Nano* **2025**, *19* (7), 7129−7139.
(18) Sun, X.; Jiang, W.-Y.; Du, P.; Gong, X.; Li, S.; Guo, Q.; Wei, J.; Shen, H. Atomically Precise Cu12 Nanoclusters with Thermally Activated Delayed Fluorescence Properties. *Inorg. Chem.* **2025**, *64* (1), 716−722.
(19) Yuan, P.; He, T.; Zhou, Y.; Yin, J.; Zhang, H.; Zhang, Y.; Yuan, X.; Dong, C.; Huang, R.; Shao, W.; Chen, S.; Song, X.; Zhou, R.; Zheng, N.; Abulikemu, M.; Eddaoudi, M.; Bayindir, M.; Mohammed, O. F.; Bakr, O. M. Hybrid Thermally Activated Nanocluster Fluorophores for X-Ray Scintillators. *ACS Energy Lett.* **2023**, *8*, 5088−5097.
(20) Diniz, A. M.; Crucho, C. I. C.; Ruedas-Rama, M. J.; Orte, A.; Dias, C. J.; Outis, M.; Pinto, S. N.; Faustino, M. A. F.; Berberan-Santos, M. N.; Avó, J. TADF-emitting Nanoparticles for Application as Probes in Time-resolved Imaging and $^1O_2$ Photosensitizers. *Adv. Opt. Mater.* **2025**, *13* (2), 2402063.
(21) Chen, G.; Cao, Y.; Tang, Y.; Yang, X.; Liu, Y.; Huang, D.; Zhang, Y.; Li, C.; Wang, Q. Advanced Near-Infrared Light for Monitoring and Modulating the Spatiotemporal Dynamics of Cell Functions in Living Systems. *Adv. Sci. (Weinh.)* **2020**, *7* (8), 1903783.
(22) Gupta, R. K.; Mohan, B.; Wang, Z.; Yang, Y.; Sun, D. Atomically Precise Metal Nanoclusters: Emerging Materials for near-Infrared II Photoluminescence. *Acc. Chem. Res.* **2026**, *59* (3), 476−486.
(23) Yuan, Z.-R.; Wang, Z.; Han, B.-L.; Zhang, C.-K.; Zhang, S.-S.; Zhu, Z.-Y.; Yu, J.-H.; Li, T.-D.; Li, Y.-Z.; Tung, C.-H.; et al. Ag_{22} Nanoclusters with Thermally Activated Delayed Fluorescence Protected by Ag/Cyanurate/Phosphine Metallamacrocyclic Monolayers through in-Situ Ligand Transesterification. *Angew. Chem., Int. Ed. Engl.* **2022**, *61* (45), No. e202211628.
(24) Bodiuzzaman, M.; Murugesan, K.; Yuan, P.; Maity, B.; Sagadevan, A.; Malenahalli H, N.; Wang, S.; Maity, P.; Alotaibi, M. F.; Jiang, D.-E.; Abulikemu, M.; Mohammed, O. F.; Cavallo, L.; Rueping, M.; Bakr, O. M. Modulating Decarboxylative Oxidation Photocatalysis by Ligand Engineering of Atomically Precise Copper Nanoclusters. *J. Am. Chem. Soc.* **2024**, *146* (39), 26994−27005.
(25) Lai, W.-F.; Wong, W.-T.; Rogach, A. L. Development of Copper Nanoclusters for in Vitro and in Vivo Theranostic Applications. *Adv. Mater.* **2020**, *32* (9), No. e1906872.
(26) Zhang, L. L.-M.; Wong, W.-Y. Atomically Precise Copper Nanoclusters as Ultrasmall Molecular Aggregates: Appealing Compositions, Structures, Properties, and Applications. *Aggregate (Hoboken)* **2023**, *4*, No. e266.
(27) Baghdasaryan, A.; Bürgi, T. Copper Nanoclusters: Designed Synthesis, Structural Diversity, and Multiplatform Applications. *Nanoscale* **2021**, *13* (13), 6283−6340.
(28) Gupta, R.; Agrawal, S.; Rai, S.; Sarkar, J.; Kumari, S.; Shil, D.; Mukherjee, S. Photoinduced Formation and Intercluster Conversion of a Thiol-Templated Copper Nanocluster. *ACS Appl. Opt. Mater.* **2024**, *2*, 1880−1890.
(29) Chakraborty, S.; Mukherjee, S. Role of Small Moiety of a Large Ligand: Tyrosine Templated Copper Nanoclusters. *J. Phys. Chem. Lett.* **2021**, *12* (13), 3266−3273.
(30) Mahato, P.; Mandal, K.; Agrawal, S.; Chopra, D.; Mukherjee, S. In Situ Crystallization, Differential Growth, and Multicolor Emission of Silver Nanoclusters. *J. Phys. Chem. Lett.* **2024**, *15* (2), 461−470.
(31) Li, H.; Kang, X.; Zhu, M. Superlattice Assembly for Empowering Metal Nanoclusters. *Acc. Chem. Res.* **2024**, *57* (21), 3194−3205.
(32) Biswas, S.; Negishi, Y. A Comprehensive Analysis of Luminescent Crystallized Cu Nanoclusters. *J. Phys. Chem. Lett.* **2024**, *15* (4), 947−958.
(33) Zhao, H.; Zhang, C.; Han, B.; Wang, Z.; Liu, Y.; Xue, Q.; Tung, C.-H.; Sun, D. Assembly of Air-Stable Copper(I) Alkynide Nanoclusters Assisted by Tripodal Polydentate Phosphoramide Ligands. *Nat. Synth.* **2024**, *3* (4), 517−526.
(34) Dong, C.; Huang, R.-W.; Chen, C.; Chen, J.; Nematulloev, S.; Guo, X.; Ghosh, A.; Alamer, B.; Hedhili, M. N.; Isimjan, T. T.; Han, Y.; Mohammed, O. F.; Bakr, O. M. $[Cu_{36}H_{10}(PET)_{24}(PPh_3)_6Cl_2]$ Reveals Surface Vacancy Defects in Ligand-Stabilized Metal Nanoclusters. *J. Am. Chem. Soc.* **2021**, *143* (29), 11026−11035.
(35) Jin, R.; Zeng, C.; Zhou, M.; Chen, Y. Atomically Precise Colloidal Metal Nanoclusters and Nanoparticles: Fundamentals and Opportunities. *Chem. Rev.* **2016**, *116* (18), 10346−10413.
(36) Fu, H.; Gao, X.; Zhang, X.; Ling, L. Recent Advances in Nonclassical Crystallization: Fundamentals, Applications, and Challenges. *Cryst. Growth Des.* **2022**, *22* (2), 1476−1499.
(37) Takano, S.; Hamasaki, Y.; Tsukuda, T. X-Ray Crystallographic Visualization of a Nucleation and Anisotropic Growth in Thiolate-Protected Gold Clusters: Toward Targeted Synthesis of Gold Quantum Needles. *J. Am. Chem. Soc.* **2025**, *147* (37), 33953−33962.
(38) Mahato, P.; Mandal, K.; Paria, K.; Chopra, D.; Mukherjee, S. Micro-Ring Morphology of Ag7NCs and Light-Induced Reversible Interconversion of FCC Ag_{14}NCs via Cu^{2+} Ions-Mediated Particle-Assisted Reversible Interconversion. *Angew. Chem., Int. Ed. Engl.* **2024**, *63* (40), No. e202409141.
(39) Alhilaly, M. J.; Huang, R.-W.; Naphade, R.; Alamer, B.; Hedhili, M. N.; Emwas, A.-H.; Maity, P.; Yin, J.; Shkurenko, A.; Mohammed, O. F.; Eddaoudi, M.; Bakr, O. M. Assembly of Atomically Precise Silver Nanoclusters into Nanocluster-Based Frameworks. *J. Am. Chem. Soc.* **2019**, *141* (24), 9585−9592.
(40) Sardar, A.; Wang, Y.; Mazumder, A.; He, G.; Gianopoulos, C. G.; Kirschbaum, K.; Jin, R. High-Yield Synthesis of Cu_{29} Nanoclusters and Their Applications in Photothermal Conversion and Catalysis. *Inorg. Chem.* **2025**, *64* (35), 17687−17695.

https://doi.org/10.1021/acs.jpclett.6c01437
J. Phys. Chem. Lett. XXXX, XXX, XXX−XXX

(41) Du, Y.; Wang, P.; Fang, Y.; Zhu, M. Asymmetric Charge Distribution in Atomically Precise Metal Nanoclusters for Boosted CO_2 Reduction Catalysis. *ChemSusChem* **2025**, *18* (6), No. e202402085.
(42) Padre, S. M.; Kiruthika, S.; Mundinamani, S.; Ravikirana; Surabhi, S.; Jeong, J.-R.; Eshwarappa, K. M.; Murari, M. S.; Shetty, V.; Ballal, M.; S C, G. Mono- and Bimetallic Nanoparticles for Catalytic Degradation of Hazardous Organic Dyes and Antibacterial Applications. *ACS Omega* **2022**, *7* (39), 35023−35034.
(43) Jara, Y. S.; Mekiso, T. T.; Washe, A. P. Highly Efficient Catalytic Degradation of Organic Dyes Using Iron Nanoparticles Synthesized with Vernonia Amygdalina Leaf Extract. *Sci. Rep.* **2024**, *14* (1), 6997.
(44) Chadha, U.; Selvaraj, S. K.; Ashokan, H.; Hariharan, S. P.; Mathew Paul, V.; Venkatarangan, V.; Paramasivam, V. Complex Nanomaterials in Catalysis for Chemically Significant Applications: From Synthesis and Hydrocarbon Processing to Renewable Energy Applications. *Adv. Mater. Sci. Eng.* **2022**, *2022*, 1−72.
(45) Biswas, S.; Pal, A.; Jena, M. K.; Hossain, S.; Sakai, J.; Das, S.; Sahoo, B.; Pathak, B.; Negishi, Y. Luminescent Hydride-Free $[Cu_7(SC_5H_9)_7(PPh_3)_3]$ Nanocluster: Facilitating Highly Selective C-C Bond Formation. *J. Am. Chem. Soc.* **2024**, *146* (30), 20937−20944.
(46) Liu, L.-J.; Zhang, M.-M.; Deng, Z.; Yan, L.-L.; Lin, Y.; Phillips, D. L.; Yam, V. W.-W.; He, J. NIR-II Emissive Anionic Copper Nanoclusters with Intrinsic Photoredox Activity in Single-Electron Transfer. *Nat. Commun.* **2024**, *15* (1), 4688.
(47) Vilar-Vidal, N.; Rivas, J.; López-Quintela, M. A. Size Dependent Catalytic Activity of Reusable Subnanometer Copper(0) Clusters. *ACS Catal.* **2012**, *2* (8), 1693−1697.
(48) Sharma, P.; Kar, S.; Sahu, M.; Ganguly, M. Copper-Based Nanoparticles for the Removal of the Crystal Violet Dye via Degradation and Adsorption: A Comparative Account. *RSC Adv.* **2025**, *15* (34), 27995−28020.
(49) Agrawal, S.; Shil, D.; Gupta, A.; Mukherjee, S. Superstructures of Copper Nanoclusters as NIR TADF Emitters: Solvent-Dependent Optical and Morphological Modulation. *Nanoscale* **2024**, *16* (44), 20556−20569.
(50) Veerakumar, P.; Salamalai, K.; Thanasekaran, P.; Lin, K.-C. Simple Preparation of Porous Carbon-Supported Ruthenium: Propitious Catalytic Activity in the Reduction of Ferrocyanate(III) and a Cationic Dye. *ACS Omega* **2018**, *3* (10), 12609−12621.
(51) Pesika, N. S.; Stebe, K. J.; Searson, P. C. Relationship between Absorbance Spectra and Particle Size Distributions for Quantum-Sized Nanocrystals. *J. Phys. Chem. B* **2003**, *107* (38), 10412−10415.
(52) Agrawal, S.; Rai, S.; Mahato, P.; Ali, A.; Mukherjee, S. Assemble-Disassemble-Reassemble Dynamics in Copper Nanocluster-Based Superstructures. *J. Phys. Chem. Lett.* **2024**, *15* (18), 4880−4889.
(53) Mahato, P.; Thomas, A. S.; Yadav, R.; Rai, S.; Shekhar, S.; Mukherjee, S. Solvent-Induced Modulation in the Optical Properties of Copper Nanoclusters and Revealing the Isomeric Effect of Templates. *Chem. Asian J.* **2023**, *18* (16), No. e202300442.
(54) Rai, S.; Agrawal, S.; Mukherjee, S. Intracellular Subdegree Temperature Sensing and Dynamics by Thermoresponsive Silver Nanoclusters as Molecular Probes. *J. Phys. Chem. Lett.* **2025**, *16*, 9316−9324.
(55) Chen, Y.; Yang, T.; Pan, H.; Yuan, Y.; Chen, L.; Liu, M.; Zhang, K.; Zhang, S.; Wu, P.; Xu, J. Photoemission Mechanism of Water-Soluble Silver Nanoclusters: Ligand-to-Metal-Metal Charge Transfer vs Strong Coupling between Surface Plasmon and Emitters. *J. Am. Chem. Soc.* **2014**, *136* (5), 1686−1689.
(56) Stamplecoskie, K. G.; Kamat, P. V. Size-Dependent Excited State Behavior of Glutathione-Capped Gold Clusters and Their Light-Harvesting Capacity. *J. Am. Chem. Soc.* **2014**, *136* (31), 11093−11099.
(57) Lei, Z.; Zhou, J.; Liang, M.; Xiao, Y.; Liu, Z. Aggregation-Induced Emission of Au/Ag Alloy Nanoclusters for Fluorescence Detection of Inorganic Pyrophosphate and Pyrophosphatase Activity. *Front. Bioeng. Biotechnol.* **2021**, *8*, 628181.
(58) Rani, D.; Singh, G.; Sharma, S. Reactions of $MoCl_5$ and MoO_2Cl_2 with 4-Phenylimidazole-2-Thiol and 2-Thiazoline-2-Thiol. *Orient. J. Chem.* **2020**, *36* (6), 1096−1102.
(59) Chen, T.; Yao, Q.; Nasaruddin, R. R.; Xie, J. Electrospray Ionization Mass Spectrometry: A Powerful Platform for Noble-Metal Nanocluster Analysis. *Angew. Chem., Int. Ed. Engl.* **2019**, *58* (35), 11967−11977.
(60) Housecroft, C. E.; Constable, E. C. TADF: Enabling Luminescent Copper(i) Coordination Compounds for Light-Emitting Electrochemical Cells. *J. Mater. Chem. C* **2022**, *10* (12), 4456−4482.
(61) Ni, F.; Zhu, Z.; Tong, X.; Xie, M.; Zhao, Q.; Zhong, C.; Zou, Y.; Yang, C. Organic Emitter Integrating Aggregation-Induced Delayed Fluorescence and Room-Temperature Phosphorescence Characteristics, and Its Application in Time-Resolved Luminescence Imaging. *Chem. Sci.* **2018**, *9* (28), 6150−6155.
(62) Zhang, L. L.-M.; Zhou, G.; Zhou, G.; Lee, H.-K.; Zhao, N.; Prezhdo, O. V.; Mak, T. C. W. Core-Dependent Properties of Copper Nanoclusters: Valence-Pure Nanoclusters as NIR TADF Emitters and Mixed-Valence Ones as Semiconductors. *Chem. Sci.* **2019**, *10* (43), 10122−10128.
(63) Jash, M.; Lu, X.; Zhou, J.; Toprak, M. S.; Sychugov, I. In Situ Transformation of Electrum Nanoclusters Embedded in Polymer Matrices Exhibit Near-infrared Emission with Quantum Yield Exceeding 70%. *Adv. Opt. Mater.* **2025**, *13* (28), e01158.
(64) Takano, S.; Hirai, H.; Nakashima, T.; Iwasa, T.; Taketsugu, T.; Tsukuda, T. Photoluminescence of Doped Superatoms $M@Au_{12}$ (M = Ru, Rh, Ir) Homoleptically Capped by $(Ph_2)PCH_2P(Ph_2)$: Efficient Room-Temperature Phosphorescence from $Ru@Au_{12}$. *J. Am. Chem. Soc.* **2021**, *143* (28), 10560−10564.
(65) Li, Q.; Zhou, D.; Chai, J.; So, W. Y.; Cai, T.; Li, M.; Peteanu, L. A.; Chen, O.; Cotlet, M.; Wendy Gu, X.; et al. Structural Distortion and Electron Redistribution in Dual-Emitting Gold Nanoclusters. *Nat. Commun.* **2020**, *11* (1), 2897.
(66) Mitsui, M.; Arima, D.; Uchida, A.; Yoshida, K.; Arai, Y.; Kawasaki, K.; Niihori, Y. Charge-Transfer-Mediated Mechanism Dominates Oxygen Quenching of Ligand-Protected Noble-Metal Cluster Photoluminescence. *J. Phys. Chem. Lett.* **2022**, *13* (40), 9272−9278.
(67) Kim, J. U.; Park, I. S.; Chan, C.-Y.; Tanaka, M.; Tsuchiya, Y.; Nakanotani, H.; Adachi, C. Nanosecond-Time-Scale Delayed Fluorescence Molecule for Deep-Blue OLEDs with Small Efficiency Rolloff. *Nat. Commun.* **2020**, *11* (1), 1765.
(68) Sanyam; Khatua, R.; Mondal, A. Cost-Effective Approach for Modeling of Multiresonant Thermally Activated Delayed Fluorescence Emitters. *J. Chem. Theory Comput.* **2023**, *19* (24), 9290−9301.
(69) Sanyam; Khatua, R.; Mondal, A. Constructing Multiresonance Thermally Activated Delayed Fluorescence Emitters for Organic LEDs: A Computational Investigation. *J. Phys. Chem. A* **2023**, *127* (49), 10393−10405.
(70) Sanyam; Tejiyan, N.; Mondal, A. Carbazole-Linked through-Space TADF Emitters for OLEDs: Tuning Photophysics *via* Molecular Architecture and Exciton Dynamics. *Mater. Adv.* **2025**, *6* (19), 6978−6990.
(71) Nikhitha; Mondal, A. Breaking the Trade-off between ΔE_{ST} and Oscillator Strength in Hybrid LR/SR-CT Compounds for Enhanced TADF Performance. *J. Mater. Chem. C* **2025**, *13* (4), 1893−1906.
(72) Gong, K.; Liu, Y.; Han, Z. Manganese-Phosphomolybdate Molecular Catalysts for the Electron Transfer Reaction of Ferricyanide to Ferrocyanide. *RSC Adv.* **2015**, *5* (58), 47004−47009.
(73) Saini, B.; Singh, S.; Mukherjee, T. K. Nanocatalysis under Nanoconfinement: A Metal-Free Hybrid Coacervate Nanodroplet as a Catalytic Nanoreactor for Efficient Redox and Photocatalytic Reactions. *ACS Appl. Mater. Interfaces* **2021**, *13* (43), 51117−51131.
(74) Chakraborty, I. N.; Roy, S.; Devatha, G.; Rao, A.; Pillai, P. P. InP/ZnS Quantum Dots as Efficient Visible-Light Photocatalysts for Redox and Carbon-Carbon Coupling Reactions. *Chem. Mater.* **2019**, *31* (7), 2258−2262.

https://doi.org/10.1021/acs.jpclett.6c01437
J. Phys. Chem. Lett. XXXX, XXX, XXX−XXX

(75) Oladoye, P. O.; Ajiboye, T. O.; Omotola, E. O.; Oyewola, O. J. Methylene Blue Dye: Toxicity and Potential Elimination Technology from Wastewater. *Results Eng.* **2022**, *16*, 100678.
(76) Sun, C.; Mammen, N.; Kaappa, S.; Yuan, P.; Deng, G.; Zhao, C.; Yan, J.; Malola, S.; Honkala, K.; Häkkinen, H.; Teo, B. K.; Zheng, N. Atomically Precise, Thiolated Copper-Hydride Nanoclusters as Single-Site Hydrogenation Catalysts for Ketones in Mild Conditions. *ACS Nano* **2019**, *13* (5), 5975−5986.
(77) Zhang, B.; Tan, X.; Zhang, Z.-H.; Liu, C.-Y.; Hu, F.; Hu, H.-S.; Chen, C.; Wang, Q.-M. Atomically Precise Copper Nanoclusters with Cu-N Interfaces toward Efficient CO_2 -to-CH_4 Electrocatalysis. *CCS Chem.* **2026**, *8*, 1122−1129.
(78) Zhao, H.; Zhang, C.; Han, B.-L.; Mahato, P.; Yang, C.-Z.; Yu, P.-X.; Wang, Z.; Tung, C.-H.; Sun, D. Gram-Scale Synthesis of an Ultrastable 38-Nuclei Copper(I) Alkynide Nanocluster for Unraveling Bifunctional Photocatalysis. *Nano Lett.* **2025**, *25* (22), 9132−9138.

https://doi.org/10.1021/acs.jpclett.6c01437
J. Phys. Chem. Lett. XXXX, XXX, XXX−XXX